ACS OMEGA

http://pubs.acs.org/journal/acsodf

Article

Performance Enhancement of an MoS_2-Based Heterojunction Solar Cell with an In_2Te_3 Back Surface Field: A Numerical Simulation Approach

Md. Hasan Ali,* Md. Abdullah Al Mamun, Md. Dulal Haque, Md. Ferdous Rahman,* M. Khalid Hossain, and Abu Zafor Md. Touhidul Islam

Cite This: *ACS Omega* 2023, 8, 7017−7029

Read Online

ACCESS | Metrics & More | Article Recommendations

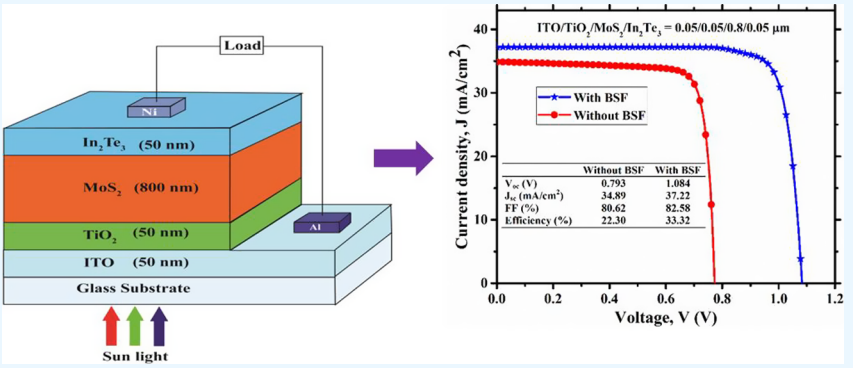

ABSTRACT: Researchers are currently showing interest in molybdenum disulfide (MoS_2)-based solar cells due to their remarkable semiconducting characteristics. The incompatibility of the band structures at the BSF/absorber and absorber/buffer interfaces, as well as carrier recombination at the rear and front metal contacts, prevents the expected result from being achieved. The main purpose of this work is to enhance the performance of the newly proposed Al/ITO/TiO_2/MoS_2/In_2Te_3/Ni solar cell and investigate the impacts of the In_2Te_3 BSF and TiO_2 buffer layer on the performance parameters of open-circuit voltage (V_{OC}), short-circuit current density (J_{SC}), fill factor (FF), and power conversion efficiency (PCE). This research has been performed by utilizing SCAPS simulation software. The performance parameters such as variation of thickness, carrier concentration, the bulk defect concentration of each layer, interface defect, operating temperature, capacitance−voltage ($C-V$), surface recombination velocity, and front as well as rear electrodes have been analyzed to achieve a better performance. This device performs exceptionally well at lower carrier concentrations (1×10^{16} cm^{-3}) in a thin (800 nm) MoS_2 absorber layer. The PCE, V_{OC}, J_{SC}, and FF values of the Al/ITO/TiO_2/MoS_2/Ni reference cell have been estimated to be 22.30%, 0.793 V, 30.89 mA/cm^2, and 80.62% respectively, while the PCE, V_{OC}, J_{SC}, and FF values have been determined to be 33.32%, 1.084 V, 37.22 mA/cm^2, and 82.58% for the Al/ITO/TiO_2/MoS_2/In_2Te_3/Ni proposed solar cell by introducing In_2Te_3 between the absorber (MoS_2) and the rear electrode (Ni). The proposed research may give an insight and a feasible way to realize a cost-effective MoS_2-based thin-film solar cell.

1. INTRODUCTION

Energy consumption and utilization have been rising with the rapid technological advancement, overpopulation, and the progression of impoverished areas around the world. Energy consumption in 2050 is expected to reach 30 terawatts (TW).[1,2] To meet the current and future global electricity demands, the manufacture of solar cells has expanded dramatically in recent years. Approximately 90% of the present photovoltaic cell market is silicon (Si)-based.[3,4] Si-based solar cells have a variety of drawbacks, including cost, weather dependence, space requirements, pollution concerns, rigidity, and high production costs.[5,6] Due to their cheap manufacturing costs, established fabrication technologies, large-scale production flexibility, and extremely effective power conversion, thin-film solar cells (TFSCs) are becoming more attractive in photovoltaic (PV) technology.[7−9] To produce cheaper, greater-efficiency, and greener solar cells, researchers in this field explore some criteria such as earth-abundant and nontoxic materials.

Received: December 8, 2022
Accepted: January 27, 2023
Published: February 8, 2023

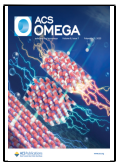

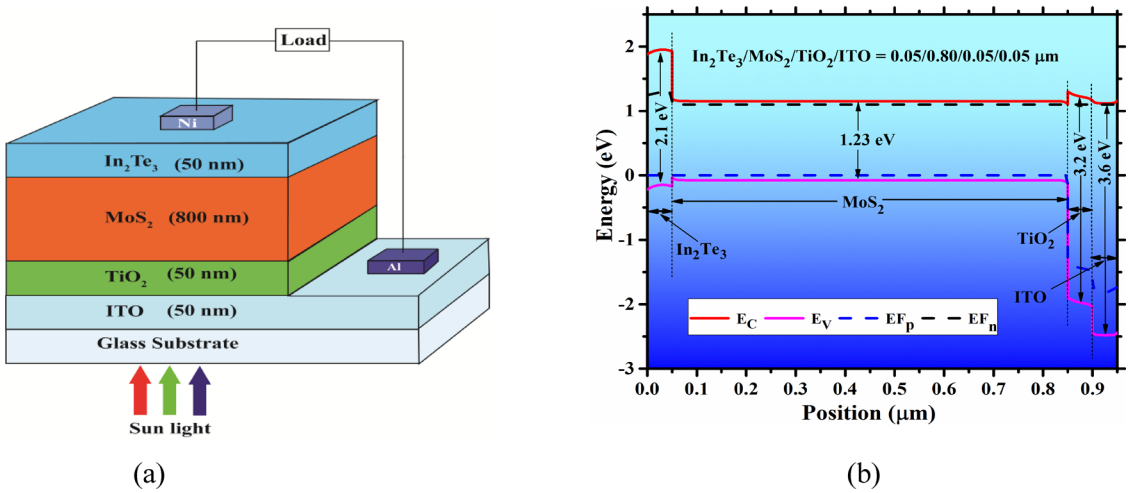

Figure 1. (a) Schematic architecture and (b) energy band alignment of the Al/ITO/TiO_2/MoS_2/In_2Te_3/Ni solar cell.

The three most popular thin film solar cells on the market are a-Si, CdTe, and CIGS. Various a-Si-, CdTe-, and CIGS-based TFSC structures have been developed practically and numerically to improve the performance of PV cells.[10−12] The highest practical efficiency of α-Si, CdTe, and CIGS has been recorded at 13.6, 22.3, and 22.1%, respectively.[13] Copper zinc tin sulfide (CZTS) is an earth-abundant solar cell material and a replacement for CIGS.[14] The highest theoretical efficiency has been recorded at 30.79%.[15]

Recently, transition metal dichalcogenides (TMDs) have been getting attraction due to their remarkable optical and electrical features such as tunable bandgap, large absorption coefficient, and suitable transportation of electrons.[16−18] TMD compounds having monolayer structures, for example, MX_2, where M, transition metal atom (Mo, W, Nb, Ti), and X, Chalcogen atom, (S, Se, Te) have gained popularity for their use in PV cells.[19,20] Furthermore, 2D materials with distinct crystal structures may help build a strong hetero-junction with excellent interfacial properties that are not affected by lattice mismatch.[21] The bandgap of molybdenum disulfide (MoS_2) varies from indirect to direct, increasing from 1.2 to 1.8 eV, indicating that the bandgap of MoS_2 is flexible as well as has multiple benefits in optoelectronics.[22] MoS_2 has an absorption coefficient of around 2.8×10^6 cm^{-1} with a statistical uncertainty of $\pm 1.3 \times 10^5$ cm^{-1}.[23] Due to these promising properties, several PV cell structures of MoS_2-based solar cells have been constructed and analyzed experimentally[24−27] and analytically[28,29] in earlier research to attain better performance.

The experimental power conversion efficiency (PCE) of the MoS_2-based Schottky-barrier solar cell (ITO/MoS_2/Au) was only 0.7 and 1.8% for the thickness of 110 and 220 nm absorber layer, respectively.[24] The same group also constructed an ITO/TiO_2/MoS_2/P_3HT/Au structure with a PCE of 1.3%.[25] The PCE of 5.23% has been achieved in a hetero-structure PV cell composed of n-MoS_2 (monolayer)/p-Si.[27] The experimental PCE of a 2-D WSe_2/MoS_2 p−n hetero-structure-based transpicuous SC has reached ∼10%.[26] A PV cell structure of ZnO/CdS/MoS_2 has exhibited a PCE of 19.62%, suggesting MoS_2 as a suitable absorber layer for solar cells.[28] The theoretical maximum efficiency of optimized ITO/ZnSe/MoS_2 and ITO/ZnSe/MoS_2/SnS photovoltaic cells has been observed as 19.48 and 21.39%, respectively.[29]

The present determined performance parameters V_{OC}, J_{SC}, fill factor (FF), and PCE of the MoS_2 SC are not able to compete with other heterojunction TFSCs. The carrier recombination at the junction may reduce V_{OC} and J_{SC}. Moreover, the inadequate carrier transportation, accumulation at the electrodes, and carrier recombination at the junction due to the absence of back surface field (BSF) or HTL and buffer layer cause the reduction of the V_{OC} and J_{SC}, which results in degradation of conversion efficiency.[30,31] The conventional MoS_2 SCs need to be remodeled for achieving better performance by inserting a suitable buffer and BSF between the absorber layer and rear electrode. The buffer layer in the SC is positioned between the window and absorber, which together form a p−n junction. It eliminates defects as well as interfacial strain caused by the window layer.[32] Therefore, it is crucial to continue further research work to attain enhanced performance of the TFSCs based on the MoS_2 absorber layer. The redesigning of the MoS_2 SC with a suitable BSF or buffer layer is very much essential. The BSF layer with desirable physical, optical, and chemical stability will facilitate proper transportation and accumulation of photogenerated carriers (PGCs) from the absorber layer to the metal electrodes. In this case, rather than using a CdS or ZnSe buffer layer, we consider using an n-type TiO_2 layer for MoS_2-based TFSCs to get better performance. It is an inert, nontoxic, and safe substance with exceptional better performance. The BSF layer has been developed in this study with 50 nm-thick indium telluride (In_2Te_3) in the molybdenum disulfide (MoS_2) solar cell, because of its ability to accumulate holes more effectively as well as reduces electron−hole recombination. Furthermore, the placement of BSF between the absorber and rear electrode can minimize the absorber layer thickness, minimizing the PV cell's overall cost.[33,34]

In this article, the photovoltaic performance parameters of the proposed (ITO/TiO_2/MoS_2/In_2Te_3) MoS_2-based thin-film heterojunction SC without and with BSF have been analyzed utilizing the SCAPS-1D simulator. The investigation of the influence of the thickness, carrier concentration, defect density, working temperature, band alignment, rear electrode, capacitance−voltage ($C-V$), and back surface recombination velocity (SRV) on SC output parameters has been performed for optimizing the device structure as well as to determine better photoconversion efficiency in a cost-effective way.

https://doi.org/10.1021/acsomega.2c07846
ACS Omega 2023, 8, 7017−7029

2. DEVICE CONSTRUCTION AND SIMULATION METHODOLOGY

To explore the newly constructed ITO/TiO_2/MoS_2/In_2Te_3 photovoltaic cell, the one-dimensional Solar Cell Capacitance Simulator (SCAPS) application has been used for simulation purposes. Promising software named SCAPS-1D was developed at the Electronic and Information Systems Department of the University of Ghent, Belgium. It may be used to predict as well as examine the optoelectronic characteristics of PV cell structures by solving fundamental equations such as electrostatic potential and continuity equation under steady-state conditions.[35] Up to seven semiconductor material layers in a solar cell may be examined in the most recent version, SCAPS 3.8, which was released in May 2020.

Figure 1a illustrates the heterojunction TFSC structure of the Al/ITO/TiO_2/MoS_2/In_2Te_3/Ni. The p-type MoS_2 absorber layer is sandwiched between the highly doped p^+-type In_2Te_3 BSF and n-type TiO_2 buffer layer to form a $p^+-p-n-n^+$ structure. A p-type absorber layer, highly doped p^+-type In_2Te_3 BSF, n-type TiO_2 buffer, and ITO window layer compose the proposed PV cell. The energy position of the p^+-In_2Te_3 BSF layer and the n-TiO_2 buffer layer is significantly greater than that of the MoS_2 absorber layer, as represented in Figure 1b.

The In_2Te_3 BSF has a larger conduction band than the MoS_2 absorber, and the conduction band minimum (CBM) is determined to be 0.87 eV between BSF and absorber. It is employed to transmit photogenerated holes (PGHs) while preventing photogenerated electrons (PGEs) from passing into back contact (Ni). The difference in bandgap between n-TiO_2 and p-MoS_2 has been determined to be 1.97 eV. The TiO_2 buffer layer intends to convey PGEs into the front contact while preventing PGHs.

In our device structure, the spike band offset of the n-type TiO_2 buffer layer has a marginally higher CBM than the p-type MoS_2 absorber, and the difference in conduction band offset (CBO) is +0.2 eV. According to a previous report, CBO between +0.2 and +0.5 eV at the absorber/Buffer junction is advantageous.[36]

SCAPS requires input data for each layer to be simulated. The sources of these input data are listed in Table 1. The parameters for ITO, TiO_2, MoS_2, and In_2Te_3 were collected from earlier theoretical simulations and experimental published articles.[28,29,37−40] The thermal velocity of electrons and holes in each layer has been estimated to be 10^7 cm/s for the sake of simplicity in the numerical analysis. Nickel (Ni) and aluminum (Al) have been used as rear and front electrodes. Table 2 depicts information on the front and rear electrodes. Table 3 represents the list of interface parameters used for Al/ITO/TiO_2/MoS_2/In_2Te_3/Ni photovoltaic cell investigation.

This numerical approach evaluates energy bands, carrier generation and recombination rate, quantum efficiency (QE), and $J-V$ characteristics at a particular operating condition using the poison and continuity equations. In addition, the simulation software appears to look into the influence of varying thickness, doping concentration, and the defect concentration of each layer, defect density at the junction, working temperature and SRV on performance parameters like V_{OC}, J_{SC}, FF, and PCE.

All simulations have been conducted using single solar irradiation of 100 mW/cm^2 under AM 1.5G spectrum at a working temperature of 300 K. The series and shunt resistances have been fixed at 10^6 and 0.5 Ω cm^{-2} correspondingly.

Table 1. Simulation-Related Input Data for MoS_2-Based TFSC at 300 K

parameters	ITO[37]	TiO_2[38]	absorber MoS_2[39]	In_2Te_3 BSF[40]
thickness (nm)	50	10−500	200−2000	10−500
E_g (eV)	3.6	3.2	1.23	2.10
χ (eV)	4	4	4.2	3.47
ε_r	9	9	4	12
N_C (cm^{-3})	2.2×10^{18}	1×10^{19}	7.5×10^{17}	1×10^{16}
N_V (cm^{-3})	1.8×10^{19}	1×10^{19}	1.8×10^{18}	1×10^{17}
μ_e (cm^2 V^{-1} s^{-1})	100	0.02	100	1000
μ_h (cm^2 V^{-1} s^{-1})	25	2	150	200
N_D (cm^{-3})	10^{18}	$10^{12}-10^{19}$	0	0
N_A (cm^{-3})	0	0	$10^{13}-10^{19}$	$10^{12}-10^{19}$
type of defect (cm^{-3})		single-acceptor	single-donor	single-donor
energetic distribution		Gaussian	Gaussian	Gaussian
defect density (cm^{-3})		$10^{12}-10^{18}$	$10^{12}-10^{18}$	10^{14}
capture cross section of electrons (cm^{-2})		1×10^{-17}	1×10^{-15}	1×10^{-15}
capture cross section of holes (cm^{-2})		1×10^{-15}	1×10^{-17}	1×10^{-17}

Table 2. Data for Electrodes Used in the Simulation

contact parameters	front electrode	back electrode
Φ (eV)	4.06; Al (110)	5.35; Ni (111)
SRV of electrons (cm/s)	10^1-10^8	10^1-10^8
SRV of holes (cm/s)	10^1-10^8	10^1-10^8

Table 3. Data for Interface Parameters Used in the MoS_2-Based Solar Cell

parameters	In_2Te_3/MoS_2 interface	MoS_2/TiO_2 interface
defect type	neutral	neutral
σ_e (cm^2)	1×10^{-20}	1×10^{-20}
σ_h (cm^2)	1×10^{-20}	1×10^{-20}
E_r	0.06	0.06
total defect density (cm^{-2})	$10^{10}-10^{17}$	$10^{10}-10^{17}$
working temperature (K)	275−475	

3. RESULTS AND DISCUSSION

3.1. Influence of Performance Parameters Due to Variation Thickness and Carrier Concentration of the MoS_2 Absorber Layer. The thickness and carrier concentration of the absorber layer are crucial factors for the improvement of the thin-film PV cell's efficiency. They affect photocarrier generation and the extraction. The rates of carrier generation and recombination increase as the absorber layer thickness increase. For analyzing the impact of the absorber layer thickness as well as carrier concentration on photovoltaic performance parameters of our designed cells, the parameters of other layers have been kept constant. The carrier concentration and thickness of the MoS_2 absorber layer have been changed from 10^{13} to 10^{19} cm^{-3} and 200 to 2000 nm, correspondingly as illustrated in Figure 2. For the thickness range of 100 to 400 nm with increasing doping 10^{13} to 10^{16} cm^{-3}, there is a slight increase in V_{OC}, which then starts to decrease from 10^{17} to 10^{18} cm^{-3}. For the thickness range of 500 to 2000 nm with increasing carrier concentration from 10^{13} to 10^{15} cm^{-3}, there is a rise in V_{OC}, whereas for the carrier concentration from 10^{16} to 10^{18} cm^{-3} there is a decline in V_{OC}. The value of J_{SC} increases as the

https://doi.org/10.1021/acsomega.2c07846
ACS Omega 2023, 8, 7017−7029

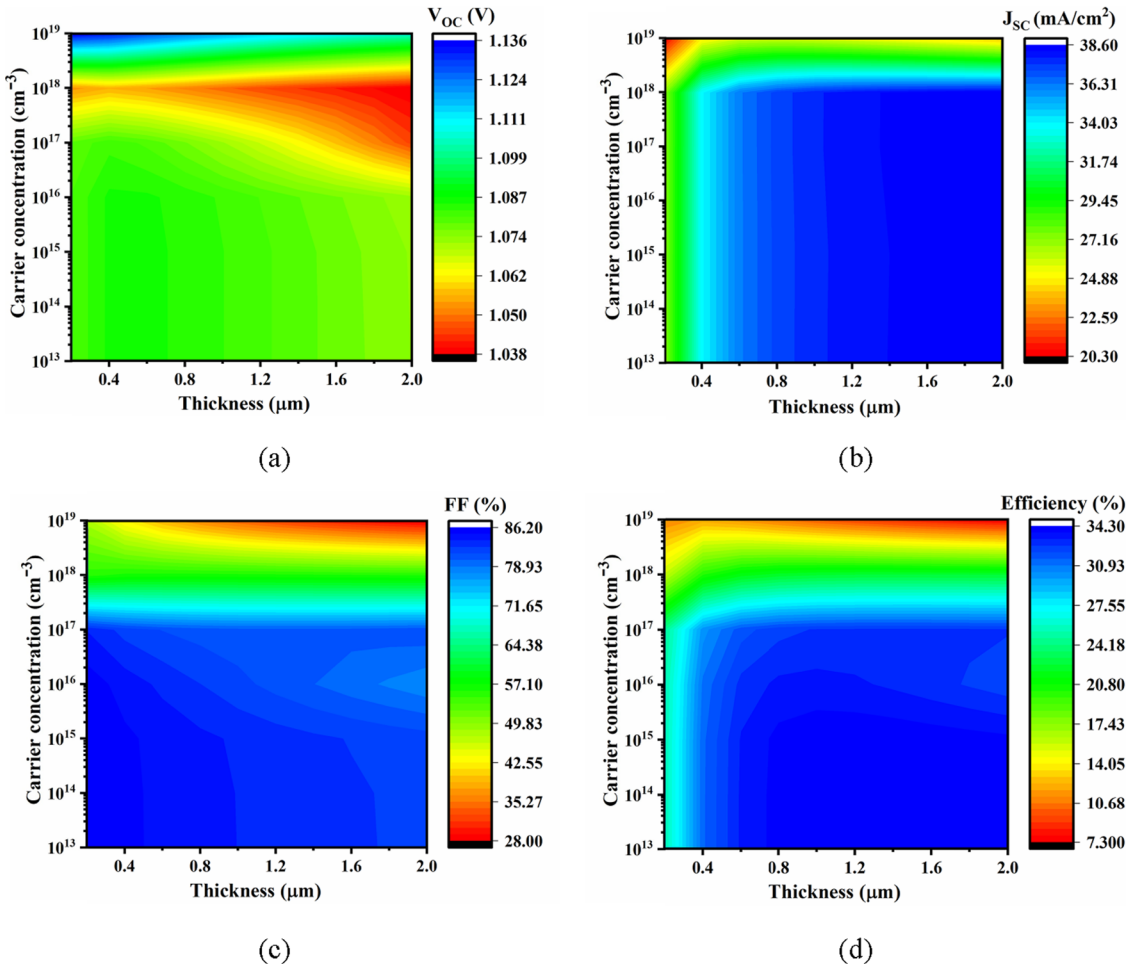

Figure 2. Concurrent impact of photovoltaic performance parameters due to variation of absorber thickness and carrier concentration (a) V_{OC} (b) J_{SC} (c) FF, and (d)η.

MoS_2 thickness rises from 200 to 2000 nm with increasing doping 10^{13} to 10^{18} cm^{-3} as illustrated in Figure 2b. The absorption of longer wavelength photons rises as the thickness of MoS_2 grows, which results in a rise in J_{SC}. The longer diffusion lengths of charge carriers are affected by the larger absorber layer, which enhances photogenerated carrier recombination via SRH recombination. The charge carriers may recombine before arriving at the charge accumulating metal contact if the absorber is too thick.[41] The lifetime of light -induced electrons shortens as the acceptor carrier concentration raises that limiting collection of carriers at the interface as a result, J_{SC} reduces.[42] Due to high carrier concentration (>10^{18} cm^{-3}) of the MoS_2 absorber layer, J_{SC} starts to decrease. The FF also reduces with the enhancement of the doping density (>10^{16} cm^{-3}) with lower thickness (>1000 nm) in MoS_2 absorber layer as represented in Figure 2c. The PCE decreases due to the combined reduction of the J_{SC} and FF at higher doping density (>10^{16} cm^{-3}) and absorber layer thickness (>1000 nm). The PCE is similarly shown to be approximately independent of MoS_2 carrier concentration until 10^{16} cm^{-3} but rapidly drops if MoS_2 carrier concentration exceeds 10^{16} cm^{-3}. This occurrence might be caused due to the rise in recombination rate as well as collisions between PGCs at greater carrier concentrations as demonstrated in Figure 2d.[43] Another explanation is that when the concentration rises, the J_{SC} begins to fall due to a decrease in minority carrier diffusion length. There is also the commencement of heavy doping effects, in which the dark current increases rather than decreases as it does at lower doping levels. As a result, the dark current starts to rise.[44] The optimal PCE of 33.32% has been achieved at MoS_2 layer thickness and carrier concentration of 800 nm and 10^{16} cm^{-3}, respectively for reducing the device fabrication cost.

3.2. Impact of Performance Due to Variation of Thickness and Defects Density of MoS_2 Absorber Layer. To examine the influence of defect density on the performance of the solar cell, the defect density and thickness of the MoS_2 absorber layer have been changed from 10^{12} to 10^{18} cm^{-3} and 200 to 2000 nm, respectively, as illustrated in Figure 3. When the defect density of MoS_2 is more than 10^{14} cm^{-3}, the solar cell performance parameters degrade significantly. For changing the bulk defect density and absorber layer thickness from 10^{12} to 10^{18} cm^{-3} and 200−2000 nm, the PCE, FF, J_{SC}, and V_{OC} of ITO/TiO_2/MoS_2/In_2Te_3 structures drops from 36.5 to 9.5%, 87 to 64%, 38.5 to 22 mA/cm^2, and 1.094 to 0.64 V respectively. When the thickness is greater than 1500 nm and the defect density is less than 10^{14} cm^{-3}, the highest V_{OC} of 1.093 V has been attained; however when the defect density is larger than 10^{14} cm^{-3}, the V_{OC} declines dramatically to 0.6342 V as represented in Figure 3a. The maximum value (38.5 mA/cm^2) of J_{SC} attained at a thickness (>1500 nm) as well as defect density (<10^{14} cm^{-3}) is demonstrated in Figure 3b. When the thickness of the absorber reduces, a sharp drop in J_{SC} may also be observed at the defect's density larger than 10^{17} cm^{-3}. The FF

https://doi.org/10.1021/acsomega.2c07846
ACS Omega 2023, 8, 7017−7029

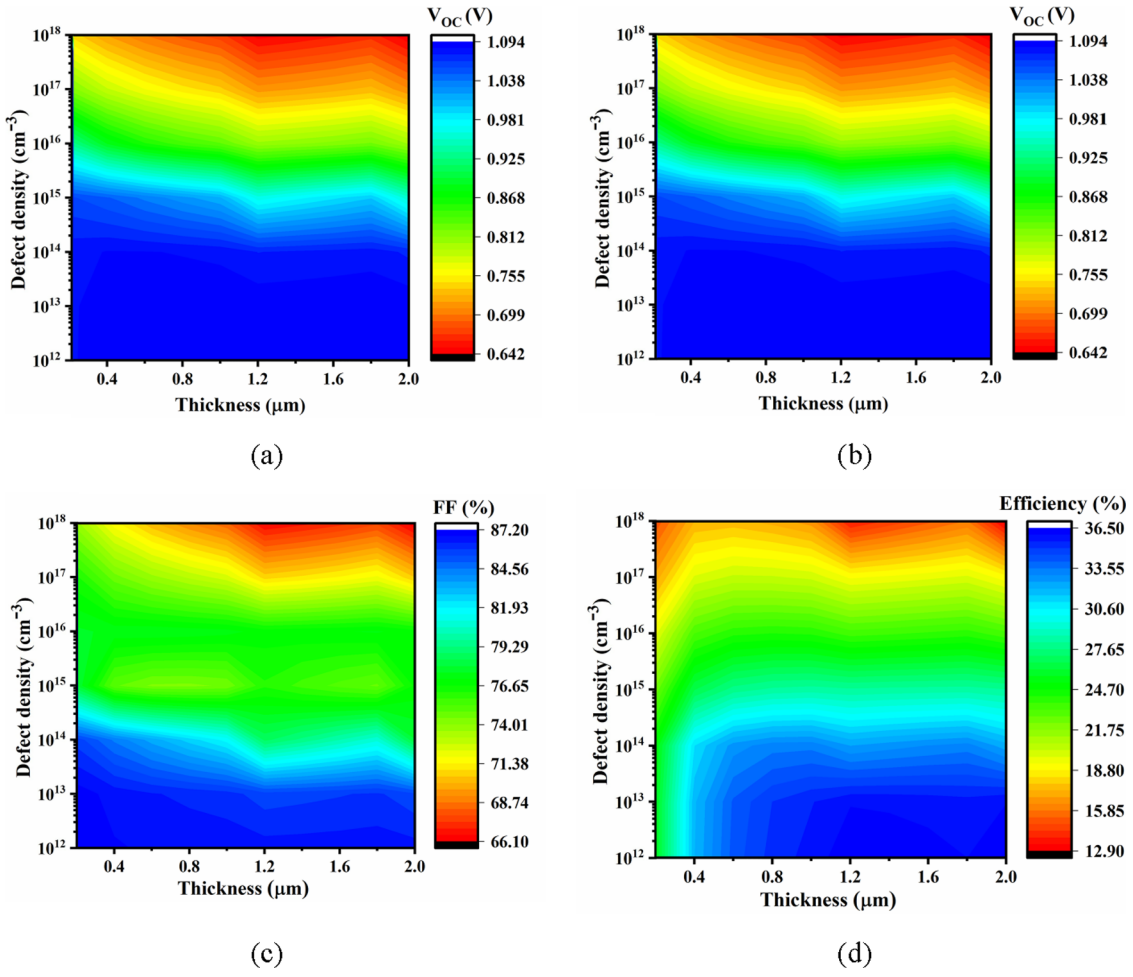

Figure 3. Concurrent impact of PV performance parameters due to variation of absorber thickness and defect density (a) V_{OC}, (b) J_{SC}, (c) FF, and (d) η.

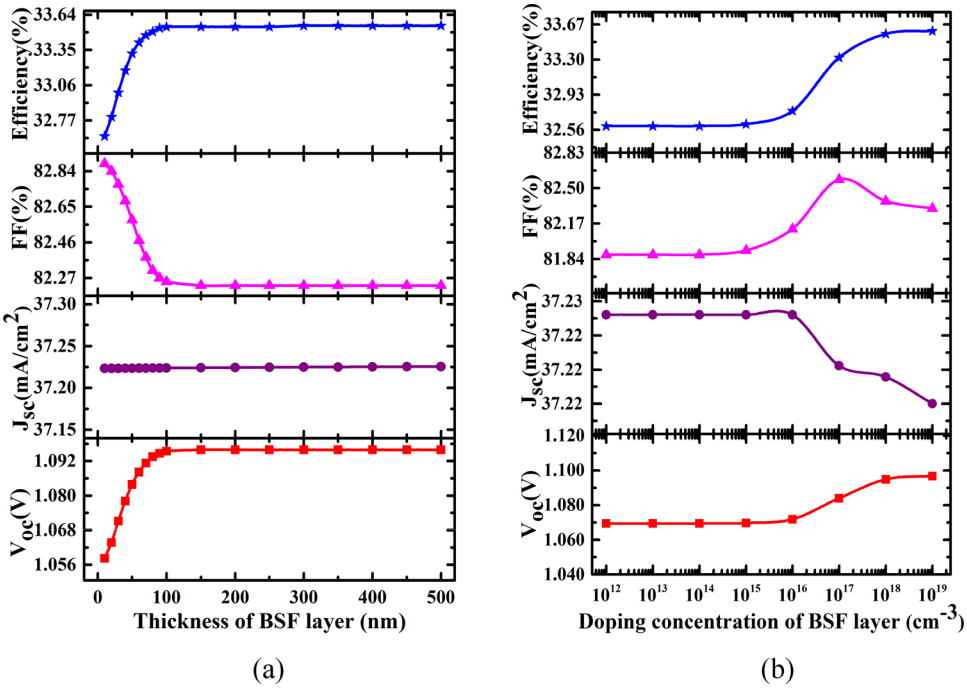

Figure 4. Impact of the PV parameter due to variation of (a) In_2Te_3 layer thickness and (b) doping concentration of the In_2Te_3 layer.

https://doi.org/10.1021/acsomega.2c07846
ACS Omega 2023, 8, 7017−7029

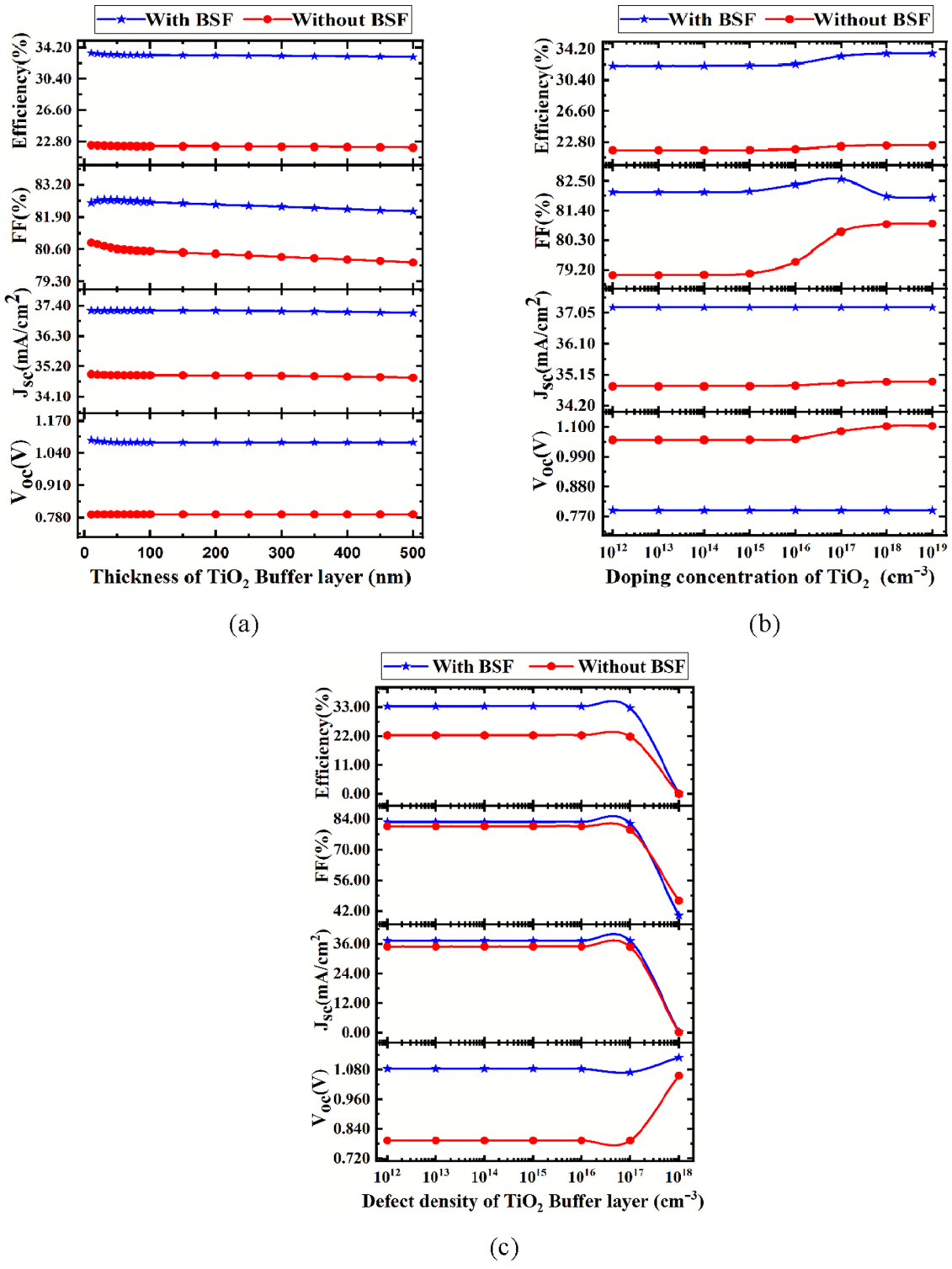

Figure 5. Impact of the PV parameter due to variation of (a) TiO_2 layer thickness (b) doping concentration in TiO_2, and (c) defect density in the TiO_2 buffer layer.

behaves in the same way as V_{OC} as illustrated in Figure 3c. The highest value (>32%) of conversion efficiency has been achieved in the thickness range of 400−2000 nm and defect density (up to 10^{14} cm^{-3}) as illustrated in Figure 3d.

The presence of defects in the MoS_2 absorber layer increases the SRH recombination rate, which decreases the number of PGCs, which assists in decreasing the value of V_{OC}, J_{SC}, FF, and PCE.[45] The optimized value of PCE 33.33% has been determined including V_{OC} of 1.0893 V, J_{SC} of 37.223 mA/cm^2, and FF of 82.58% at constant thickness of 800 nm MoS_2 absorber layer and defect concentration of 10^{14} cm^{-3}.

3.3. Effect of Thickness and Carrier Concentration of In_2Te_3 BSF on Performance Parameters. By establishing a strong field near the rear electrode, the back surface field (BSF) has been utilized to maximize SC efficiency by reducing SRV.

https://doi.org/10.1021/acsomega.2c07846
ACS Omega 2023, 8, 7017−7029

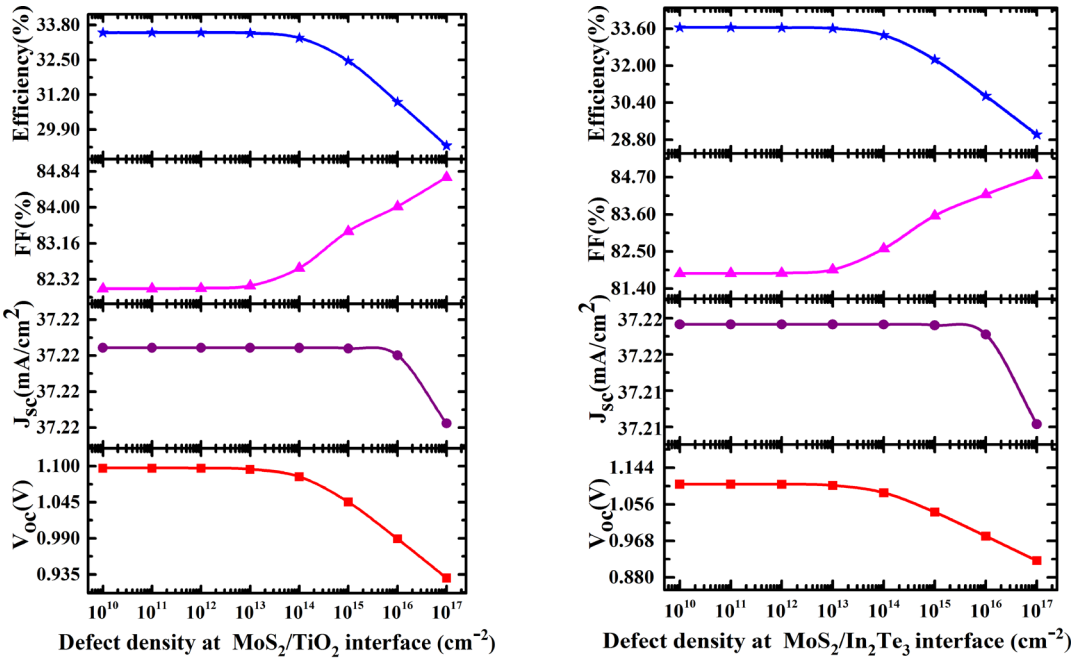

Figure 6. Influence of defect at (a) MoS_2/TiO_2 and (b) MoS_2/In_2Te_3 interfaces on PV parameters.

The influence of the thickness and doping concentration of the In_2Te_3 BSF on the device's performance has been evaluated.

The In_2Te_3 BSF layer's thickness has been changed from 10 to 500 nm at 1×10^{17} cm^{-3} acceptor doping concentration for analyzing the impact on device performance parameters as illustrated in Figure 4a.

As the In_2Te_3 BSF layer thickness increases, device performance begins to deteriorate. The main reason for this degradation is that the enhancement of BSF thickness causes a rise in series resistance. This increase in resistance due to the BSF layer thickness affects the FF and PCE of a device.[46]

Figure 4b depicts the effect of doping concentration of In_2Te_3 on PV parameters at a thickness of 50 nm, and the influence of carrier concentration on the In_2Te_3 BSF layer has been studied in the range of 10^{12} to 10^{19} cm^{-3}. All the PV parameters increase significantly with rising peak doping concentration starting from 10^{16} cm^{-3} excluding the J_{SC}.

Higher levels of acceptor doping concentrations generate potential at the In_2Te_3/MoS_2 junction, reducing carrier recombination loss. Due to the increased carrier concentration, the Fermi level of BSF moves toward the valence band (VB) allowing for rapid accumulation of holes at the rear electrode by developing an ohmic contact with rear-metal contact (Ni).[47] The optimal thickness and acceptor concentration have been chosen 50 nm and 10^{17} cm^{-3} for the In_2Te_3 BSF layer for reducing the device fabrication cost.

3.4. Influence of Thickness Variation, Carrier Concentration, and Defect Density of the Buffer Layer on PV Performances. The PV parameters of the MoS_2-based thin film heterojunction PV cell with and without BSF have been changed, when the buffer layer's thickness varies. The thickness changes from 10 to 500 nm. When the TiO_2 buffer layer thickness is increased, all of the PV parameters are slightly reduced for both with and without the BSF structure as illustrated in Figure 5a.

The influence of TiO_2 buffer layer doping concentration on PV parameters has also been evaluated as depicted in Figure 5b. Our findings imply that all PV parameters enhances with increasing carrier concentration starting at 10^{14} cm^{-3} for the structure with BSF. The V_{OC}, J_{SC}, and PCE have been increasing from 1.0521 to 1.1042 V, 37.22331 to 37.22353 mA/cm^2, and 32.25 to 33.65%, respectively, for the doping concentrations ranging from 10^{12} and 10^{19} cm^{-3}, respectively, while V_{OC} falls from 0.7931 to 0.7928 V and J_{SC}, FF, and η rise from 34.79023 to 34.93195 mA/cm^2, 79 to 80.92% and 21.8 to 22.41% respectively for changing doping concentrations from 10^{12} and 10^{19} cm^{-3} for the structure without BSF. The increase of TiO_2 buffer layer thickness means photogenerated electrons need to flow long distances to reach the front contact, which increase the carrier recombination rate. Therefore, the number of carriers as well as PV performance parameters reduces, while the increase of doping density in TiO_2 increases the number of carriers, which contributes to increase efficiency parameter.[15] The optimum value of thickness and doping concentration has been determined to be 50 nm and 10^{17} cm^{-3}, respectively for reducing device fabrication cost.

For the n-type buffer layer, we employed single-acceptor type bulk defects. The defect density of the buffer layer TiO_2 has been changed from 10^{12} to 10^{18} cm^{-3}, whereas the layer's defect concentration remained constant at 10^{14} cm^{-3} displayed in Figure 5c. All the parameters, excluding V_{OC}, decrease rapidly with rising bulk defect density beginning from 10^{17} cm^{-3} for both with and without the BSF structure. The presence of defect density in the TiO_2 layer contributes to increase the SRH recombination rate, which degrade the overall performance of the SC.[38] The defect density has been kept at 10^{15} cm^{-3} for determining optimum performance.[38]

3.5. Impact of Interface Defect on Performance Parameters. Interface defect state impacts on the output parameters significantly similar to the bulk defects. Figure 6a,b depicts the consequence of an interfacial defect at MoS_2/TiO_2

https://doi.org/10.1021/acsomega.2c07846
ACS Omega 2023, 8, 7017−7029

and In_2Te_3/MoS_2 on the PV parameters of a newly developed MoS_2-based solar cell. The interface defect concentration for both MoS_2/TiO_2 and In_2Te_3/MoS_2 interfaces has been varied from 10^{10} to 10^{17} cm^{-2} in this numerical analysis, while the other parameters remained fixed. It has been noticed from Figure 6a,b for both interfaces that all the PV parameters degrade significantly with increasing defect density starting from 10^{14} cm^{-2}. The PCE decreased from 33.65 to 29.02% and 32.52 to 29.02% for changing defect concentration from 10^{10} to 10^{17} $cm^{-2}$for the In_2Te_3/MoS_2 and MoS_2/TiO_2 respectively. To obtain optimal PV performance of MoS_2 solar cells, defect density has been kept 10^{14} cm^{-2} for both interfaces. The trap states present at the interface act as a recombination center, which contribute to the reduction of the number of photo-generated carriers as well as inhibit the carrier collection.[48] Both of these interface state-related defects contribute to a significant reduction in performance parameters.

3.6. Impact of Temperature on Cell Performance. The working temperature of the proposed MoS_2-based photovoltaic cell must be regulated to achieve stability as demonstrated in Figure 7. The PV parameters of MoS_2-based heterojunction with

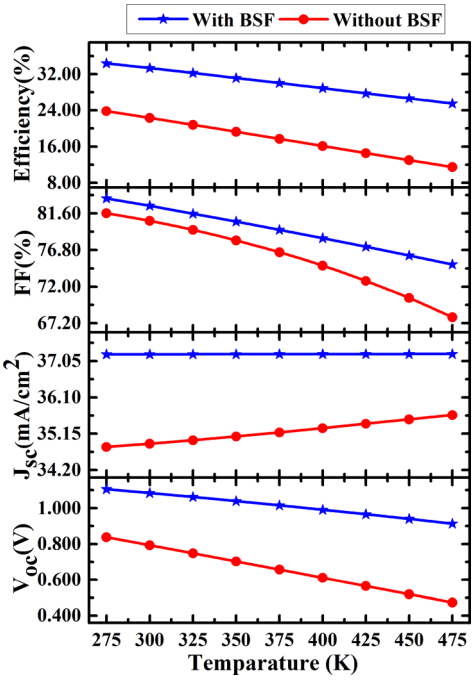

Figure 7. Influence of performance parameters due to variation of working temperature in MoS_2-based SC with and without BSF.

and without BSF are considerably reduced when the temperature increases from 275 to 475 K. The PCE of $ITO/TiO_2/MoS_2/In_2Te_3$ and $ITO/TiO_2/MoS_2$ structures is determined to be 34.36 and 23.79%, respectively at 275 K, but it falls to 25.45 and 11.46%, respectively due to the rise in operating temperature at 475 K.

These simulation results also represent that a MoS_2 solar cell with BSF has better thermal consistency than a structure without BSF.[37] At high temperatures, more electron−hole pairs are generated for a given irradiance that maintains a constant value of J_{SC}. The rise in the working temperature causes to reduce band gap of MoS_2 and the reverse saturation current also enhances, which results in a decrease in V_{OC}, FF, and efficiency. In the previous publications, the consequences of PCE degradation as working temperatures were generally well acknowledged in refs 49−51.

When the temperature of PV solar cell rises, the height of the bandgap energy shrinks, resulting in a small increase of J_{SC}. As a result, the solar cells V_{OC} would be reduced. As a result, the reduction of V_{OC} as well as insignificant rise of J_{SC} leads to a fall in FF and PCE of the photovoltaic cells at higher temperature.[51]

3.7. Study of the Influence of SRV on the Performance Parameters. The influence of SRV at the rear contact on the performance characteristics of our proposed photovoltaic cell has been analyzed in detail as shown in Figure 8. We have alternated the SRV without and with BSF structure from 10^1 to 10^8 cm/s. All the PV parameters of $ITO/TiO_2/MoS_2$ degrade significantly with increasing SRV. The recombination of electron and holes happens at higher SRV before reaching metal contact. By inserting an addition layer called BSF, it is possible to overcome this problem. Figure 8a illustrates that the FF and PCE of $ITO/TiO_2/MoS_2/In_2Te_3$ structure increase with increasing SRV and at the same time V_{OC} and J_{SC} remain constant. The minority carrier's lifetime as well as diffusion length has been dramatically reduced because of the rapid recombination of electrons and holes at high SRV, resulting in a decline in PV performance parameters.[47] The photons with low energy absorb in the thick absorber layer despite having a high SRV; it helps to achieve a high FF and PCE because of the high absorption coefficient.[52]

The external quantum efficiency (EQE) curve is shown in Figure 8b, at three distinct SRV: 10^2, 10^8 cm/s (without In_2Te_3), and 10^7 cm/s (with In_2Te_3). At higher SRV, the EQE of the solar cell structure without In_2Te_3 reduces compared with the solar cell with In_2Te_3 at longer wavelength at higher SRV. As the rate of SRV rises, the electron and hole begin to recombine at the rear contact surface due to the absence of In_2Te_3 degrading the solar cell performance parameters.[37]

3.8. Effect of Capacitance−Voltage (*C*−*V*) on Solar Cell. The $C-V$ analysis has been performed in the range of frequency from 0.5 kHz to 1 MHz to investigate the consistency of the results. The depletion and diffusion capacitances are associated with the p−n junctions. The value of depletion capacitance is larger than diffusion capacitance at reverse bias voltage, whereas the diffusion capacitance dominates at the forward bias.

The capacitance of the p−n junction solar cell is found to be 16 nF cm^{-2} at the zero bias voltage as demonstrated in Figure 9a. The capacitance rises exponentially with the enhancement of the polarization potential at particular frequency. The insensitiveness of the absorber traps at any frequencies shows this tendency. At the reverse bias, the effective traps do not help to minimize the effective charge, which results in reduced capacitance.[53]

The Mott−Schottky plot of the $Al/ITO/TiO_2/MoS_2/In_2Te_3/Ni$ PV cell has been represented in Figure 9b. The flat-band potential of the proposed SC originates from the intersection of the $1/C^2$ plot with the voltage axis. The negative slope of the plot indicates that holes are majority carriers as well as the space charge area largely occupies the p-type MoS_2 layer. The high carrier density in the MoS_2 layer may have originated from the PGCs owing to the exposure of sunlight. The marginal deviation for $1/C^2$ may be as a consequence of the localized deep states in the absorber layer. The impact of the deep states is not dominant and the main effect is caused by the modulation of the majority carriers.[53]

https://doi.org/10.1021/acsomega.2c07846
ACS Omega 2023, 8, 7017−7029

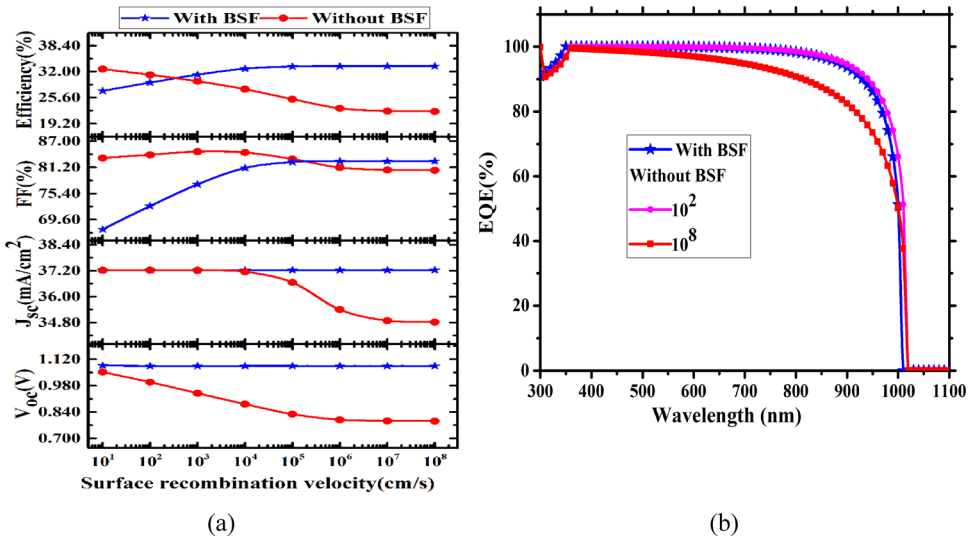

Figure 8. Impact of surface recombination velocity function on (a) performance parameters and (b) EQE.

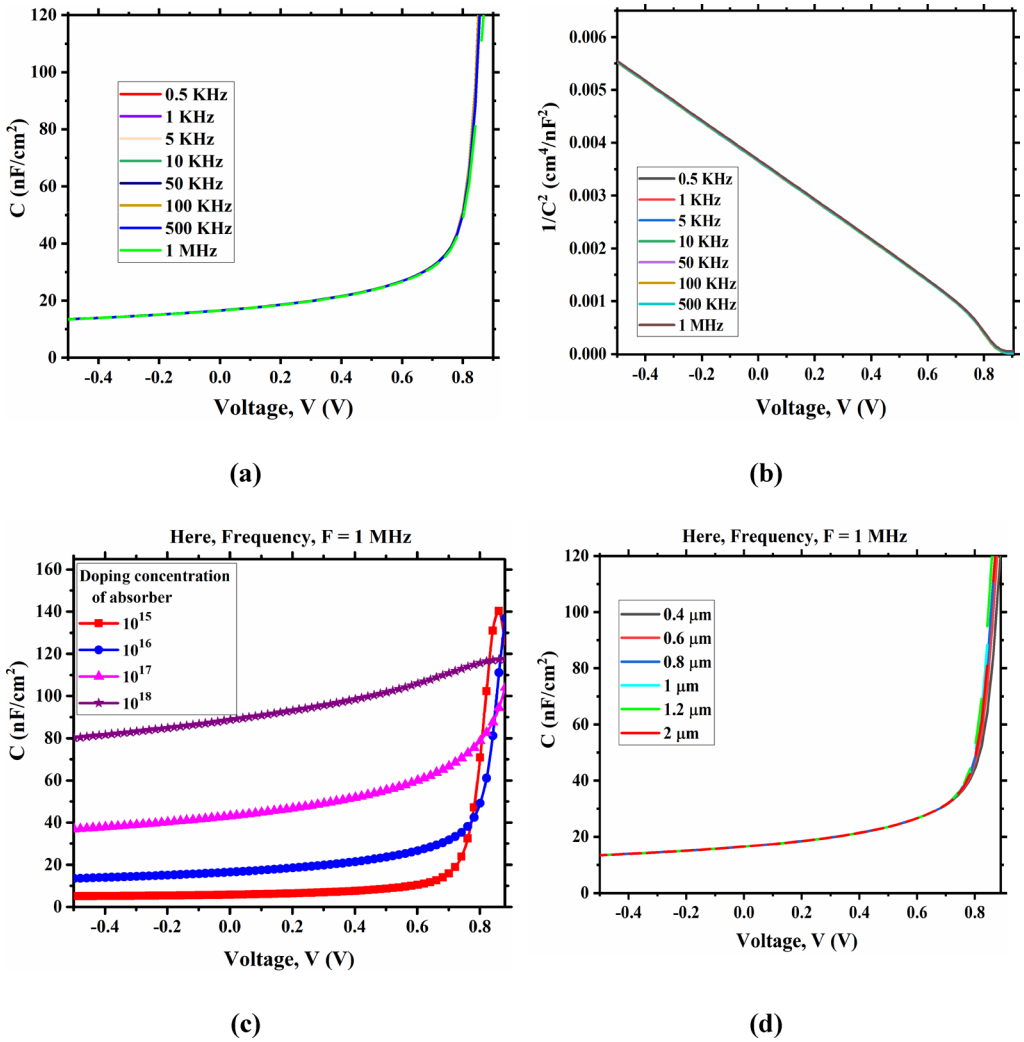

Figure 9. Effect of $C-V$ on solar cell (a) varying frequency, (b) $1/C^2-V$ curve, (c) varying doping of absorber, and (d) varying thickness of absorber.

Figure 9c represents $C-V$ properties of MoS_2 SC due to the variation of the absorber layer doping concentration. The value of capacitances increases with the rise of the forward bias voltage and act as Mott−Schottky junctions. The lower value of the built-in potential originated from Mott−Schottky plot under the illumination of sunlight, which can be assigned to the capacitance developed from the photogenerated carrier in side lower mobility materials. The rise of doping density enhances

https://doi.org/10.1021/acsomega.2c07846
ACS Omega 2023, 8, 7017−7029

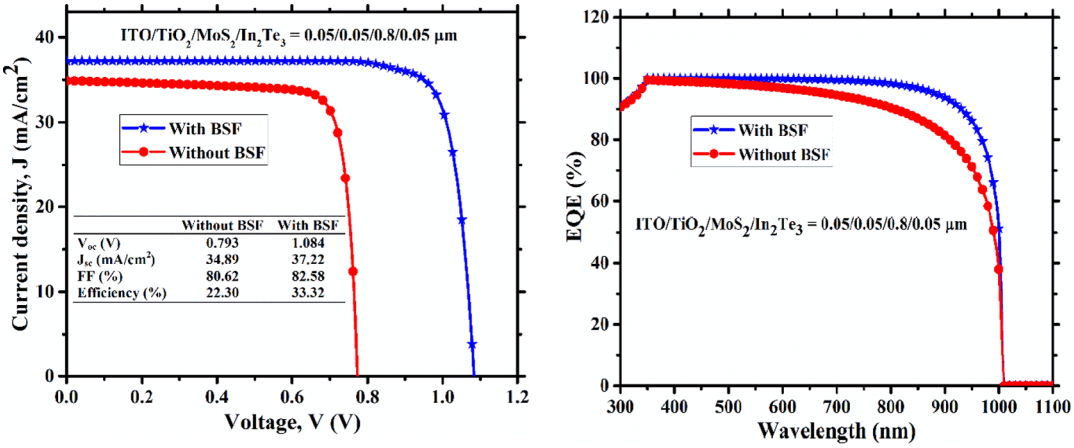

Figure 10. (a) $J-V$ curve and (b) EQE curve of the cell designed with and without the BSF structure.

the charge accumulation at the interface, which contributes to the rise of the value of capacitance, which is reported in a previous study.[54]

Figure 9d demonstrates the change of capacitance due to the change of bias voltage at different thicknesses at a constant frequency of 1 MHz. The value of capacitance change due to the variation of thickness is almost insignificant. After the voltage of 0.80 V, the value of capacitance rises dramatically with the increase of voltage. The same type tendency of the capacitance on the thickness and voltage has been published in the previous article.[55]

3.9. Device Output Performance. The simulated current density−voltage ($J-V$) and EQE curves for the optimized MoS_2-based photovoltaic cell with and without BSF layer have been demonstrated in Figure 10 under the 1.5AM solar illumination. The estimated values of the V_{OC}, J_{SC}, FF, and PCE is 1.084 V, 37.22 mA/cm^2, 82.58%, and 33.32% of the proposed Al/ITO/TiO_2/MoS_2/In_2Te_3/Ni heterostructure PV cell determined from numerical simulation.

The output parameters of Al/ITO/TiO_2/MoS_2/Ni structure have been found to be 0.793 V, 34.89 mA/cm^2, 80.62%, and 22.30%. The determined PV parameters from the numerical simulation of the SC with In_2Te_3 are much higher than those of the structure without BSF.

The $J-V$ curve is a powerful tool to estimate the recombination loss of the carrier in the SC. The introduction of In_2Te_3 BSF in the proposed SC structure results in a lower value of recombination current density. In addition, it has been demonstrated that the total minority carrier recombination current density of MoS_2 solar cell with In_2Te_3 BSF layer estimated to be smaller than that of the reference SC. The simulated results indicate that photogenerated carriers reflected back toward the MoS_2/TiO_2 rather than recombination at the back contact. Therefore, the inclusion of the In_2Te_3 BSF layer in the reference Al/ITO/TiO_2/MoS_2/Ni structure contributes to enhanced performance parameters by reducing carrier recombination loss.[56]

Furthermore, the efficiency enhancement may be justified by calculating the lattice mismatch between absorber and BSF layer (Table 4) using the following equation:[15,57]

$$\delta = 2|a_s - a_e|/(a_s + a_e)$$

where, δ, a_s, and a_e are the lattice mismatch, substrate, and epitaxial thin film lattice constant, respectively.

Table 4. Lattice Mismatch between Absorber/BSF Values Have Been Compared with Lattice Mismatch (%) of the BSFs or HTLs Employed in the Previous Studies

	lattice parameters			
layer	a (Å)	B (Å)	C (Å)	lattice mismatch
MoS_2	3.15	3.15	12.3	
In_2Te_3	13.417	13.417	13.417	8.69%
SnS	3.82	3.82	6.257	19.22%
Sb_2S_3	11.31	3.8363	11.22	19.64%

The value of the lattice constant for the different materials has been taken from previous research.[58−60] The lattice mismatch of MoS_2 and In_2Te_3 is 8.69%, which is lower than that of the HTLs employed in the previous studies. The primary cause of non-radiative recombination is the presence of defect and interface defect density, which results in carrier losses and a drop in output voltage.[61] The lower value of lattice mismatch between In_2Te_3 and MoS_2 results in the reduction of interface defect density as well as recombination loss significantly. Thus, the insertion of the In_2Te_3 BSF layer in MoS_2 reference enhances the performance parameters significantly. The absence of BSF in the Al/ITO/TiO_2/MoS_2/Ni reference structure exhibits low V_{OC} due to the rise of minority carrier recombination. As a result, the device's performance parameters have been affected.

Figure 10b shows the EQE of both the optimized cells. High EQE has been demonstrated for the proposed solar cell with In_2Te_3 compared to the without In_2Te_3 structure. The insertion of the In_2Te_3 BSF layer in the proposed SC structure decreases the PGC recombination by creating strong back surface electric fields at the In_2Te_3/MoS_2 interface and enhances the absorption edge at the higher wavelength range, which contribute to maximize the overall performance parameters of the SC.[37]

Table 5 compares the evolution of MoS_2-based solar cell configurations investigated by various research groups. The PCE increases from 19.62 to 21.39% according to the earlier reported experimental and numerical simulations. In comparison to the published values, the improved V_{OC}, J_{SC}, and PCE have been achieved by this numerical simulation. The presence of deep-level defect levels inside the MoS_2 absorber's energy band gap as

https://doi.org/10.1021/acsomega.2c07846
ACS Omega 2023, 8, 7017−7029

Table 5. Upgraded Performance Parameters Values Have Been Compared with Previously Published Reports[a]

number	type of analysis	formation of cell	MoS_2 depth (nm)	J_{SC} (mA/cm^2)	V_{OC} (mV)	FF (%)	η (%)	ref
01	Exp.	ITO/MoS_2	110				0.7	24
02	Exp.	ITO/MoS_2	220				1.8	24
03	Exp.	ITO/TiO_2/MoS_2/P_3HT		4.7	560	–	1.3	25
04	Exp.	n-MoS_2 (monolayer)/p-Si		22.32	410	57.26	5.23	27
05	Exp.	WSe_2/MoS_2					∼10	26
06	Theo.	n-ZnO/n-CdS/p-MoS_2	1000				19.62	28
07	Theo.	ITO/n-ZnSe/p-MoS_2		27.84	820	84.6	19.48	29
08	Theo.	ITO/n-ZnSe/p-MoS_2/p^+-SnS	1000	29.89	841	85	21.39	29
09	Theo.	Al/FTO/n-CdS/p-MoS_2/Ni	1000	34.11	760	82.80	21.61	62
10	Theo.	Al/FTO/CdS/MoS_2/p^+-Sb_2S_3/Ni	1000	35.20	920	85.51	27.96	62
11	Theo.	ITO/TiO_2/MoS_2	800	34.89	793	80.62	22.30	this work
12	Theo.	ITO/TiO_2/MoS_2/In_2Te_3	800	37.22	1084	82.58	33.32	this work

[a]Exp. = experimental work and Theo. = theoretical work.

well as interface-associated defects degrades the performance parameters of the previously published structures. The practical performance of MoS_2 photovoltaic cells was quite poor compared to the numerically determined values. The carrier recombination at the rear and front contact and misalignment of bands at the BSF/absorber and absorber/buffer is also responsible for the reduction. The high surface carrier recombination at MoS_2/back contact results in a lower value of the efficiency parameters. The P^+-type In_2Te_3 BSF layer introduced between an absorber and a back contact layer acts as a passivation layer and enhances the efficiency parameters V_{OC}, J_{SC}, FF, and PCE by reducing the minority carrier recombination loss. Moreover, the formation of p^+−p junction creates strong electric field along the MoS_2 absorber layer due to the insertion of the In_2Te_3 BSF layer, which reflect the photo-generated carriers toward the front contact and enhances the overall efficiency parameters.

4. CONCLUSIONS

A comparative analysis of the performance parameters of MoS_2-based TFSCs with and without an In_2Te_3 BSF layer has been done in this numerical simulation using SCAPS-1D. Instead of the utilization of conventional toxic cadmium sulfide (CdS) as a buffer layer, TiO_2 with optimum thickness has been employed as a buffer layer material. The optimal thicknesses for the TiO_2 buffer layer, MoS_2 absorber layer, and In_2Te_3 BSF layer have been chosen to be of 50, 800, and 50 nm, respectively. The optimized values of carrier concentration have also been selected to be approximately to 10^{17}, 10^{16}, 10^{17} cm^{-3}, respectively. The peak defect concentration in the p-MoS_2 absorber layer and the interface defect at MoS_2/TiO_2 and In_2Te_3/MoS_2 have been calculated to be 10^{14} eV^{-1} cm^{-3} and 10^{14} cm^{-2} and 10^{14} cm^{-2}, correspondingly. The numerically simulated determined value PCE is 33.32%, including V_{OC} of 1.084 V, J_{SC} of 33.22 mA/cm^2, and FF of 82.58% of the suggested MoS_2-based heterojunction with the In_2Te_3, which is greater than that without In_2Te_3 PV cell. The present research work provides guidelines for the realization of a highly efficient MoS_2-based PV cell in a cost-effective way.

AUTHOR INFORMATION

Corresponding Authors

Md. Hasan Ali − *Department of Electrical and Electronic Engineering, Begum Rokeya University, Rangpur, Rangpur 5400, Bangladesh*; Email: hasan@brur.ac.bd

Md. Ferdous Rahman − *Department of Electrical and Electronic Engineering, Begum Rokeya University, Rangpur, Rangpur 5400, Bangladesh*; orcid.org/0000-0002-0090-2384; Email: ferdous@brur.ac.bd

Authors

Md. Abdullah Al Mamun − *Department of Electrical and Electronic Engineering, Begum Rokeya University, Rangpur, Rangpur 5400, Bangladesh*

Md. Dulal Haque − *Department of Electronics and Communication Engineering, Hajee Mohammad Danesh Science and Technology University, Dinajpur 5200, Bangladesh*

M. Khalid Hossain − *Institute of Electronics, Atomic Energy Research Establishment, Bangladesh Atomic Energy Commission, Dhaka 1349, Bangladesh*; orcid.org/0000-0003-4595-6367

Abu Zafor Md. Touhidul Islam − *Department of Electrical and Electronic Engineering, Rajshahi University, Rajshahi 6205, Bangladesh*

Complete contact information is available at: https://pubs.acs.org/10.1021/acsomega.2c07846

Notes

The authors declare no competing financial interest.

ACKNOWLEDGMENTS

The authors would like to express their sincere gratitude to Dr. Marc Burgelman and his colleagues at the EIS Department at the University of Gent in Belgium for providing us with the opportunity to conduct research using the SCAPS-1D software.

LIST OF ABBREVIATIONS

MoS_2	molybdenum disulfide
In_2Te_3	indium telluride
TiO_2	titanium dioxide
ITO	indium tin oxide
BSF	back surface field
V_{OC}	open circuit voltage
J_{SC}	short circuit current
FF	fill factor
PCE	power conversion efficiency
C−V	capacitance−voltage
SRV	surface recombination velocity
TMDs	transition metal dichalcogenides
CBM	conduction band minimum

https://doi.org/10.1021/acsomega.2c07846
ACS Omega 2023, 8, 7017−7029

CBO	conduction band offset
TW	terawatts
TFSCs	thin-film solar cells
SC	solar cell
PV	photovoltaic
CdTe	cadmium telluride
CIGS	copper indium gallium selenide
CZTS	copper zinc tin sulfide
HTL	hole transport layer
PGC	photogenerated carrier
PGHs	photogenerated holes
PGEs	photogenerated electrons
EQE	external quantum efficiency
CdS	cadmium sulfide
SRH	Shockley−Read−Hall

REFERENCES

(1) Meissner, D. *Solar Power Implications of Our Climate Crisis*, 2020; pp 2−3.

(2) Matin Bhuiyan, M. A. Development of High Efficiency Ultra-Thin CdTe Solar Cell with Back Surface Field. Ph.D. Thesis, Univ. Kebangs, Malaysia, 2011.

(3) Andreani, L. C.; Bozzola, A.; Kowalczewski, P.; Liscidini, M.; Redorici, L. Silicon Solar Cells: Toward the Efficiency Limits. *Adv. Phys.: X* **2019**, *4*, No. 1548305.

(4) Lee, T. D.; Ebong, A. U. A Review of Thin Film Solar Cell Technologies and Challenges. *Renewable Sustainable Energy Rev.* **2017**, *70*, 1286−1297.

(5) Alzahrani, G. S.; Alzahrani, F. S.; Nahhas, A. M. Study of the Specific Factors Effecting the PV Solar Cell's Efficiency in Saudi Arabia. *Sustain. Energy* **2020**, *8*, 6−11.

(6) Imamzai, M.; Aghaei, M.; Thayoob, Y. H. A Review on Comparison between Traditional Silicon Solar Cells and Thin-Film CdTe Solar Cell. *Proc. Natl. Grad. Conf.* **2011**, *2012*, 8−10.

(7) Green, M. A.; Hishikawa, Y.; Dunlop, E. D.; Levi, D. H.; Hohl-Ebinger, J.; Ho-Baillie, A. W. Y. Solar Cell Efficiency Tables (Version 52). *Progr. Photovolt.: Res. Appl.* **2018**, *26*, 427−436.

(8) Lee, C. T.; Lu, K. F.; Tseng, C. Y. Carrier Drift Velocity Balance Mechanism in Si-Based Thin Film Solar Cells Using Graded Microcrystalline SiGe Absorption Layer. *Sol. Energy* **2015**, *114*, 1−7.

(9) Paudel, N. R.; Wieland, K. A.; Compaan, A. D. Ultrathin CdS/CdTe Solar Cells by Sputtering. *Sol. Energy Mater. Sol. Cells* **2012**, *105*, 109−112.

(10) Mostefaoui, M.; Mazari, H.; Khelifi, S.; Bouraiou, A.; Dabou, R. Simulation of High Efficiency CIGS Solar Cells with SCAPS-1D Software. *Energy Procedia* **2015**, *74*, 736−744.

(11) Yang, J.; Banerjee, A.; Guha, S. Conversion Efficiencies Triple-Junction Amorphous Silicon Alloy Solar Cell with 14.6% Initial and 13.0% Stable Conversion Efficiencies. *Appl. Phys. Lett.* **1997**, *70*, 2975−2977.

(12) Gloeckler, M.; Sankin, I.; Zhao, Z. CdTe Solar Cells at the Threshold to 20% Efficiency. *Int. J. Photovolt.* **2013**, *3*, 1389−1393.

(13) Lee, T. D.; Ebong, A. U. A Review of Thin Fi Lm Solar Cell Technologies and Challenges. *Renewable Sustainable Energy Rev.* **2017**, *70*, 1286−1297.

(14) Katagiri, H.; Jimbo, K.; Maw, W. S.; Oishi, K.; Yamazaki, M.; Araki, H.; Takeuchi, A. Development of CZTS-Based Thin Fi Lm Solar Cells. *Thin Solid Films* **2009**, *517*, 2455−2460.

(15) Atowar Rahman, M. Enhancing the Photovoltaic Performance of Cd-Free Cu2ZnSnS4 Heterojunction Solar Cells Using SnS HTL and TiO2 ETL. *Sol. Energy* **2021**, *215*, 64−76.

(16) Choi, W.; Choudhary, N.; Han, G. H.; Park, J.; Akinwande, D.; Lee, Y. H. Recent Development of Two-Dimensional Transition Metal Dichalcogenides and Their Applications. *Mater. Today* **2017**, *20*, 116−130.

(17) Li, X.; Zhu, H. Two-Dimensional MoS2: Properties, Preparation, and Applications. *J. Mater.* **2015**, *1*, 33−44.

(18) Manzeli, S.; Ovchinnikov, D.; Pasquier, D.; Yazyev, O. V.; Kis, A. 2D Transition Metal Dichalcogenides. *Nat. Rev. Mater.* **2017**, *2*, 17033.

(19) Zaidi, B.; Shekhar, C.; Hadjoudja, B.; Gagui, S.; Chouial, B. Optimization of Highly Efficient Monolayer MoSe2 Based Solar Cells. *Acta Phys. Pol. A* **2019**, *136*, 495−497.

(20) Chhowalla, M.; Shin, H. S.; Eda, G.; Li, L. J.; Loh, K. P.; Zhang, H. The Chemistry of Two-Dimensional Layered Transition Metal Dichalcogenide Nanosheets. *Nat. Chem.* **2013**, *5*, 263−275.

(21) Wang, X.; Huang, L.; Peng, Y.; Huo, N.; Wu, K.; Xia, C.; Wei, Z.; Tongay, S.; Li, J. Enhanced Rectification, Transport Property and Photocurrent Generation of Multilayer ReSe2/MoS2 p−n Heterojunctions. *Nano Res.* **2016**, *9*, 507−516.

(22) Yang, K.; Liu, T.; Zhang, X. D. Bandgap Engineering and Near-Infrared-II Optical Properties of Monolayer MoS2: A First-Principle Study. *Front. Chem.* **2021**, *9*, 1−13.

(23) Kwak, J. Y. Absorption Coefficient Estimation of Thin MoS 2 Film Using Attenuation of Silicon Substrate Raman Signal. *Results Phys.* **2019**, *13*, No. 102202.

(24) Paquin, F.; Rivnay, J.; Salleo, A.; Stingelin, N.; Silva, C. Multi-Phase Semicrystalline Microstructures Drive Exciton Dissociation in Neat Plastic Semiconductors. *J. Mater. Chem. C* **2015**, *3*, 10715−10722.

(25) Shanmugam, M.; Bansal, T.; Durcan, C. A.; Yu, B. Molybdenum Disulphide/Titanium Dioxide Nanocomposite-Poly 3-Hexylthiophene Bulk Heterojunction Solar Cell. *Appl. Phys. Lett.* **2012**, *100*, 1−5.

(26) Cho, A. J.; Song, M. K.; Kang, D. W.; Kwon, J. Y. Two-Dimensional WSe2/MoS2 p-n Heterojunction-Based Transparent Photovoltaic Cell and Its Performance Enhancement by Fluoropolymer Passivation. *ACS Appl. Mater. Interfaces* **2018**, *10*, 35972−35977.

(27) Tsai, M. L.; Su, S. H.; Chang, J. K.; Tsai, D. S.; Chen, C. H.; Wu, C. I.; Li, L. J.; Chen, L. J.; He, J. H. Monolayer MoS2 Heterojunction Solar Cells. *ACS Nano* **2014**, *8*, 8317−8322.

(28) Rashid, H.; Rahman, K. S.; Hossain, M. I.; Tabet, N.; Alharbi, F. H.; Amin, N. Prospects of Molybdenum Disulfide (MoS2) as an Alternative Absorber Layer Material in Thin Film Solar Cells from Numerical Modeling. *Chalcogenide Lett.* **2014**, *11*, 397−403.

(29) Dey, M.; Shahriar, M. F.; Ali, A.; Dey, M.; Das, N. K. Design and Optimization of an Efficient Molybdenum Disulfide (MoS2) Solar Cell with Tin Sulfide BSF. *2nd Int. Conf. Electr. Comput. Commun. Eng. ECCE 2019*, 2019; pp 1−5.

(30) Choi, Y. C.; Seok, S. I. Efficient Sb2S3-Sensitized Solar Cells via Single-Step Deposition of Sb2S3 Using S/Sb-Ratio-Controlled SbCl3-Thiourea Complex Solution. *Adv. Funct. Mater.* **2015**, *25*, 2892−2898.

(31) Versavel, M. Y.; Haber, J. A. Structural and Optical Properties of Amorphous and Crystalline Antimony Sulfide Thin-Films. *Thin Solid Films* **2007**, *515*, 7171−7176.

(32) Eisele, W.; Ennaoui, A.; Schubert-Bischoff, P.; Giersig, M.; Pettenkofer, C.; Krauser, J.; Lux-Steiner, M.; Zweigart, S.; Karg, F. XPS, TEM and NRA Investigations of Zn(Se,OH)/Zn(OH)2 Films on Cu(In,Ga)(S,Se)2 Substrates for Highly Efficient Solar Cells. *Sol. Energy Mater. Sol. Cells* **2003**, *75*, 17−26.

(33) Cao, Y.; Zhu, X.; Chen, H.; Zhang, X.; Zhou, J.; Hu, Z.; Pang, J. Towards High Efficiency Inverted Sb2Se3 Thin Film Solar Cells. *Sol. Energy Mater. Sol. Cells* **2019**, *200*, No. 109945.

(34) Bayad, H.; El Manouni, A.; Marí, B.; Khattak, Y. H.; Ullah, S.; Baig, F. Influence of P+-ZnTe Back Surface Contact on Photovoltaic Performance of ZnTe Based Solar Cells. *Opt. Quantum Electron.* **2018**, *50*, 259.

(35) Burgelman, M.; Nollet, P.; Degrave, S. Modelling Polycrystalline Semiconductor Solar Cells. *Thin Solid Films* **2000**, *361-362*, 527−532.

(36) Minemoto, T.; Hashimoto, Y.; Satoh, T.; Negami, T.; Takakura, H.; Hamakawa, Y. Cu(In,Ga)Se2 Solar Cells with Controlled Conduction Band Offset of Window/Cu(In,Ga)Se2 Layers. *J. Appl. Phys.* **2001**, *89*, 8327−8330.

(37) Haque, M. D.; Ali, M. H.; Islam, A. Z. M. T. Efficiency Enhancement of WSe2 Heterojunction Solar Cell with CuSCN as a Hole Transport Layer: A Numerical Simulation Approach. *Sol. Energy* **2021**, *230*, 528−537.

(38) Kohnehpoushi, S.; Nazari, P.; Nejand, B. A.; Eskandari, M. MoS 2 : A Two-Dimensional Hole-Transporting Material for High-Ef Fi

https://doi.org/10.1021/acsomega.2c07846
ACS Omega 2023, 8, 7017−7029

Ciency , Low-Cost Perovskite Solar Cells. *Nanotechnology* **2018**, *29*, 205201.
(39) Mouloua, D.; Kotbi, A.; Deokar, G.; Kaja, K.; El Marssi, M.; El Khakani, M. A.; Jouiad, M. Recent Progress in the Synthesis of MoS2 Thin Films for Sensing, Photovoltaic and Plasmonic Applications: A Review. *Materials* **2021**, *14*, 3283.
(40) Dey, M.; Dey, M.; Matin, M. A.; Amin, N. High Performance and Stable Molybdenum Telluride PV Cells with Indium Telluride BSF. *ICDRET 2016 - 4th Int. Conf. Dev. Renew. Energy Technol.*, 2016; pp 4−7.
(41) Subedi, K. K.; Phillips, A. B.; Shrestha, N.; Alfadhili, F. K.; Osella, A.; Subedi, I.; Awni, R. A.; Bastola, E.; Song, Z.; Li, D. B.; Collins, R. W.; Yan, Y.; Podraza, N. J.; Heben, M. J.; Ellingson, R. J. Enabling Bifacial Thin Film Devices by Developing a Back Surface Field Using CuxAlOy. *Nano Energy* **2021**, *83*, No. 105827.
(42) Rahman, M. A. Design and Simulation of a High-Performance Cd-Free Cu2SnSe3 Solar Cells with SnS Electron-Blocking Hole Transport Layer and TiO2 Electron Transport Layer by SCAPS-1D. *SN. Appl. Sci.* **2021**, *3*, 1.
(43) Ahmmed, S.; Aktar, A.; Tabassum, S.; Rahman, M. H.; Rahman, M. F.; Abu, A. B. CuO Based Solar Cell with V2O5 BSF Layer: Theoretical Validation of Experimental Data. *Superlattices Microstruct.* **2021**, *151*, No. 106830.
(44) Zekry, A.; Shaker, A.; Salem, M. *Solar Cells and Arrays: Principles, Analysis, and Design*, 2018; vol *1*.
(45) Taheri, S.; Ahmadkhan Kordbacheh, A.; Minbashi, M.; Hajjiah, A. Effect of Defects on High Efficient Perovskite Solar Cells. *Opt. Mater.* **2021**, *111*, No. 110601.
(46) Khattak, Y. H.; Baig, F.; Toura, H.; Beg, S.; Soucase, B. M. Efficiency Enhancement of Cu2BaSnS4 Experimental Thin-Film Solar Cell by Device Modeling. *J. Mater. Sci.* **2019**, *54*, 14787−14796.
(47) Khatun, M. M.; Sunny, A.; Ahmed, S. R. A. Numerical Investigation on Performance Improvement of WS2 Thin-Film Solar Cell with Copper Iodide as Hole Transport Layer. *Sol. Energy* **2021**, *224*, 956−965.
(48) Basyoni, M. S. S.; Salah, M. M.; Mousa, M.; Shaker, A.; Zekry, A.; Abouelatta, M.; Alshammari, M. T.; Al-Dhlan, K. A.; Gontrand, C. On the Investigation of Interface Defects of Solar Cells: Lead-Based vs Lead-Free Perovskite. *IEEE Access* **2021**, *9*, 130221−130232.
(49) Bouich, A.; Hartiti, B.; Ullah, S.; Ullah, H.; Touhami, M. E.; Santos, D. M. F.; Mari, B. Experimental, Theoretical, and Numerical Simulation of the Performance of CuIn x Ga (1-x) S 2 -Based Solar Cells. *Optik* **2019**, *183*, 137−147.
(50) Biplab, S. R. I.; Ali, M. H.; Moon, M. M. A.; Pervez, M. F.; Rahman, M. F.; Hossain, J. Performance Enhancement of CIGS-Based Solar Cells by Incorporating an Ultrathin BaSi2 BSF Layer. *J. Comput. Electron.* **2020**, *19*, 342−352.
(51) Abdalmageed, H. I.; Fedawy, M.; Aly, M. H. Effect of Absorber Layer Bandgap of CIGS-Based Solar Cell with (CdS/ZnS) Buffer Layer. *J. Phys.: Conf. Ser.* **2021**, *2128*, No. 012009.
(52) Gray, J. L. *Handbook of Photovoltaic Science and Engineering*; John Wiley & Sons: New York, 2011.
(53) Gupta, G. K.; Garg, A.; Dixit, A. Electrical and Impedance Spectroscopy Analysis of Sol-Gel Derived Spin Coated Cu2ZnSnS4 Solar Cell. *J. Appl. Phys.* **2018**, *123*, No. 013101.
(54) Islam, M. S.; Sobayel, K.; Al-Kahtani, A.; Islam, M. A.; Muhammad, G.; Amin, N.; Shahiduzzaman, M.; Akhtaruzzaman, M. Defect Study and Modelling of SnX3-Based Perovskite Solar Cells with SCAPS-1D. *Nanomaterials* **2021**, *11*, 1218.
(55) Zahoo, R. K.; Saleh, A. N. Effect Of Carrier Concentration And Thickness Of Absorber Layer On Performance CBTS Solar Cell. *Turkish J. Comput. Math. Educ.* **2021**, *12*, 5056−5064.
(56) Barman, B.; Kalita, P. K. Influence of Back Surface Field Layer on Enhancing the Efficiency of CIGS Solar Cell. *Sol. Energy* **2021**, *216*, 329−337.
(57) Cang, Q.; Guo, H.; Jia, X.; Ning, H.; Ma, C.; Zhang, J.; Yuan, N.; Ding, J. Enhancement in the Efficiency of Sb2Se3 Solar Cells by Adding Low Lattice Mismatch CuSbSe2 Hole Transport Layer. *Sol. Energy* **2020**, *199*, 19−25.
(58) Ariswan; Sutrisno, H.; Prasetyawati, R. Crystal Structure, Optical, and Electrical Properties of SnSe and SnS Semiconductor Thin Films Prepared by Vacuum Evaporation Techniques for Solar Cell Applications. *IOP Conf. Ser. Mater. Sci. Eng.* **2017**, *202*, No. 012042.
(59) Molina-Sánchez, A.; Wirtz, L. Phonons in Single-Layer and Few-Layer MoS2 and WS2. *Phys. Rev. B: Condens. Matter Mater. Phys.* **2011**, *84*, No. 155413.
(60) Kondrotas, R.; Chen, C.; Tang, J. Sb2S3 Solar Cells. *Joule* **2018**, *2*, 857−878.
(61) Wang, K.; Gunawan, O.; Todorov, T.; Shin, B.; Chey, S. J.; Bojarczuk, N. A.; Mitzi, D.; Guha, S. Thermally Evaporated Cu2 ZnSnS4 Solar Cells. *Appl. Phys. Lett.* **2010**, *97*, 8−11.
(62) Haque, D.; Ali, H.; Rahman, F.; Zafor, A.; Islam, T. Numerical Analysis for the Efficiency Enhancement of MoS 2 Solar Cell: A Simulation Approach by SCAP-1D. *Opt. Mater.* **2022**, *131*, No. 112678.

https://doi.org/10.1021/acsomega.2c07846
ACS Omega 2023, 8, 7017−7029